Article

Solid-State Synthesis and Phase Transitions in the $RE_2(MoO_4)_3$ Family Monitored by Thermodiffraction

Ivan da Silva, Gerardo Gil de Cos, Cristina González-Silgo,* Javier López-Solano, Andrés Mujica, Nivaria R. Ramírez-Rodríguez, and Manuel E. Torres
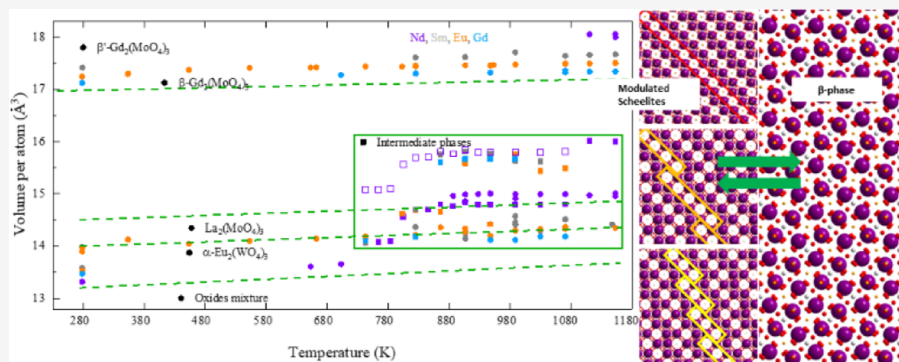
Read Online

ACCESS | Metrics & More | Article Recommendations | Supporting Information

ABSTRACT: Solid-state synthesis and phase transitions of $RE_2(MoO_4)_3$ (RE ≡ Nd, Sm, Eu, and Gd) samples have been monitored by X-ray thermodiffraction with synchrotron radiation. The experiment was divided in two stages. In the first heating, different non-stoichiometric molybdates ($Eu_4Mo_7O_{27}$, $Eu_2Mo_4O_{15}$, and $Pr_2Mo_4O_{15}$ structure types) emerged from the RE_2O_3 and MoO_3 oxides before the expected phases (with α-$Eu_2(WO_4)_3$ and $La_2(MoO_4)_3$ structure types and the β-$Gd_2(MoO_4)_3$ phase). The formation and coexistence of intermediate phases have been explained by common structural motifs with unit cell volumes per atom among those with the formula $RE_2(MoO_4)_3$. Subsequent heating−cooling cycles showed the occurrence of the reversible and reconstructive α [$La_2(MoO_4)_3$] ↔ β phase transition, including the less common transition $\beta \rightarrow \alpha$ [$La_2(MoO_4)_3$] obtained by heating the β'-$Gd_2(MoO_4)_3$ phase from room temperature and clarifying much of the controversy in the literature. The transition mechanisms were studied by proposing a common supercell and comparing the RE and vacancy ordering within similar layers of MoO_4^{2-} tetrahedra. The possible formation of stacking faults in $Nd_2(MoO_4)_3$ was explained as a mixture of modulated scheelite phases. This research supports the importance of a directed and rational synthesis analyzing the intermediate products and their phase transitions for the enrichment of materials with new or improved properties.

1. INTRODUCTION

Rare earth molybdates produced from the binary system $n_{RE_2O_3}$−m_{MoO_3} (RE ≡ La−Lu, Bi, Sc, and Y) constitute a large group of inorganic compounds of much interest due to their multifunctional properties (optical, dielectric, electronic, magnetic, catalytic, ferroic, etc.) with consequent technological applications (scintillators, solid-state lasers, Raman shifters, phosphors, electronic and ionic conductors, thermal or luminescent sensors, fuel cells, energy storage, photocatalysts, etc.).[1−5] Molybdates with composition n/m = 1:1 and chemical formula RE_2MoO_6 and those with n/m = 1:3 with the formula $RE_2(MoO_4)_3$ are the most studied. Very recent work has also been done on combined compounds with both compositions.[6]

Compounds with the chemical formula RE_2MoO_6 (1:1), also called oxymolybdates, yield two polymorphs depending on the ionic radius of the lanthanide.[7] They are known for their luminescent characteristics and for their potential as dielectrics under microwaves;[8,9] lately, they have been studied as proton conductors and as good conducting networks and ion diffusion pathways, offering sufficient active sites for catalytic conversion.[10−12] On the other hand, compounds with the formula $RE_2(MoO_4)_3$ (1:3) are of great interest in fundamental science because of the great flexibility of their crystal structures that makes possible negative thermal expansion, negative compression, phase transitions (e.g., ferroelectric−paraelectric), and other thermal and pressure-related anomalies.[13−15] At least 10

different structures are known from ambient conditions to their respective melting points and amorphization pressures;[1,15] and this great structural variety explains many of their multifunctional properties. In addition to those already mentioned, more recent and combined properties are the morphology control with biological applications and the negative thermal expansion combined with upconversion emission.[16,17]

Rare earth molybdates are conventionally prepared by solid-state reaction from stoichiometric mixtures of the oxides RE_2O_3 and MoO_3. The highest heating temperature is usually limited to approximately 923 K to avoid the vaporization of the MoO_3. Although there is information on the preparation of $RE_2(MoO_4)_3$ samples, there is still no unequivocal opinion on the conditions that favor the growth of the different crystal structures of various polymorphs. The generation of specific, sometimes metastable, phases is essentially controlled by kinetic factors.[18,19] Compounds with the same chemical composition but obtained by different preparation methods (solid-phase synthesis, growth in melt, co-precipitation from solutions, sol−gel method, hydrothermal synthesis) can show significant changes in structure under other conditions.[20]

However, since Bixner in 1979 until today, there has been quite a consensus on the assumption of the phase diagram showing the thermal stability zones versus the ionic radii of the trivalent metals.[1] All known crystalline structures in this family of compounds belong to three polytypes with no symmetry relationship.[18] Various isomorphs are distinguished and related by crystalline symmetry within each polytype. The three polytypes are:

1.1. Modulated Scheelites. The monoclinic phases are $La_2(MoO_4)_3$ (which we will refer to as the LaMo-phase)[21] and α-$Eu_2(WO_4)_3$ (which we will refer to as the α-phase).[22] These phases are derived from the $CaWO_4$ scheelite in which the cationic vacancy ($\square$), which appears in the complete formula $RE_2\square(MoO_4)_3$, is ordered in the RE (or Ca) position.[23] Other modulated structures that do not appear in the Brixner diagram have been investigated, for example, the formation of an incommensurable phase for $Pr_2(MoO_4)_3$.[24] Similar compounds have also been studied under pressure, in which a "pre-amorphous" phase appears. This is explained by the formation of stacking defects associated with the rearrangement of the rare earth and its associated vacancies.[25]

1.2. Ferroelectric−Ferroelastic. Ferroelectric−ferroelastic phases with the polar orthorhombic β'-$Gd_2(MoO_4)_3$ structure type (we will call it the β'-phase).[26] The corresponding paraelectric−paraelastic phase possesses a tetragonal β-$Gd_2(MoO_4)_3$ structure type (we will refer to it as the β-phase).[27] Before the amorphization of the β'-phase under high pressure, one or several more distorted phases have been detected, some of them referred to as the δ phase.[28]

1.3. Negative Thermal Expansion. Negative thermal expansion (NTE) phases with the orthorhombic γ-$Sc_2(WO_4)_3$ structure type (hereafter γ-phase).[29] Recently, a new polymorph that does not appear in the Brixner diagram has been reported, with the monoclinic structure of the $Fe_2(MoO_4)_3$ in compounds belonging to the solid solution $(Lu_{1-x}Eu_x)_2(MoO_4)_3$ ($0 \leq x < 0.2$).[30]

The dependence on the types and conditions of synthesis coupled with the changes introduced by the lanthanide ionic radius complicates the study of phase transformations in these systems under temperature and pressure. The transitions, with increasing temperature, LaMo-β, $\alpha-\beta$, and $\beta'-\beta$ of

$RE_2(MoO_4)_3$ (RE = La−Dy) compounds are known and are also reported in the review by Brixner and co-workers in 1979.[1] The $\beta'-\beta$ transitions, the most studied, take place between 413 and 513 K, and the $\alpha-\beta$ and LaMo-β transitions occur between 1073 and 1273 K. In both cases, the transition temperature increases with the ionic radius. There is much more controversy in the literature about the $\beta-\alpha$ (or β-LaMo) transition, recalling that the α- (or LaMo-) and β-phases are not related by symmetry and are first-order reconstructive transitions. Already, Nassau and co-authors have observed that single crystals of the ferroelectric phase (RE = Gd, Tb, Dy, Ho, and Y) were wholly transformed to the α-form in 3 days at 1073 K.[31] They observed much more stability in the ferroelectric phase of powdered $Tb_2(MoO_4)_3$, which does not completely transform to the α-phase even after 7 days at 873 K. At higher temperatures, this transition is indeed confirmed. Also, in the same work, they propose the possible appearance of the γ-phase at high temperature (at 1323 K) for $Tb_2(MoO_4)_3$. More recently, Autchin and co-authors performed a complete characterization of the α-$Eu_2(MoO_4)_3$ compound.[32] They obtained the α-phase by solid-state synthesis and detected two endothermic signals on the DSC curve at 1182 and 1438 K upon heating the sample. During cooling, the crystallization temperature at 1373 K was confirmed, but there was no second exothermic peak. However, during the following heating, the endothermic peak was reproduced at above 1173 K, and they concluded that the observed transition agrees with the $\alpha-\beta$ phase transition. Also, very recently, Tang and co-authors[33] studied changes in luminescence intensities depending on the transition temperature synthesized by solid-state reaction of three polymorphs of $Eu_2(MoO_4)_3$ regulating the sintering temperature: the scheelite phase at 873 K, a new monoclinic modulated scheelite phase between 973 and 1073 K and the β-phase between 1173 and 1273 K. They also presented DTA curves where an exothermic peak appears above 873 K, assigned to the scheelite-new modulated scheelite phase transition, and an endothermic peak near 1173 K, assigned to the newly modulated scheelite-β transition.[33]

While we were working on this manuscript, Popov and co-authors[20] published a work on the formation and evolution of the local and long-range structures in almost the entire $RE_2(MoO_4)_3$ series (with RE ≡ La, Pr, Nd, Eu, Gd, Dy, Ho, and Yb) using XRD with synchrotron radiation, Raman, infrared, and photoluminescence spectroscopies and simultaneous thermal analysis with ICP spectroscopy. They prepared the samples by co-precipitation with subsequent calcination of the precursors. They found that all molybdates initially crystallized with the monoclinic crystal structure of a modulated scheelite in the superspace group $I112/b$. When the calcination time increases, a significant rearrangement of the crystal structure occurs, which mainly depends on the lanthanide type. These authors reviewed and proposed a new phase diagram for this family according to the newly observed phase sequence.[20]

There is less knowledge about other m/n compositions of the $m_{RE_2O_3}-n_{MoO_3}$ system. The discovery of the fast ionic conductivity in the $La_2Mo_2O_9$ compound (m/n = 1:2), together with the determination of its structure, is relatively recent.[34] Since the last decade, this has stimulated further research to determine new structures with other very close compositions, e.g., $RE_5Mo_3O_{16.5}$ (m/n = 5:6).[35,36] On the
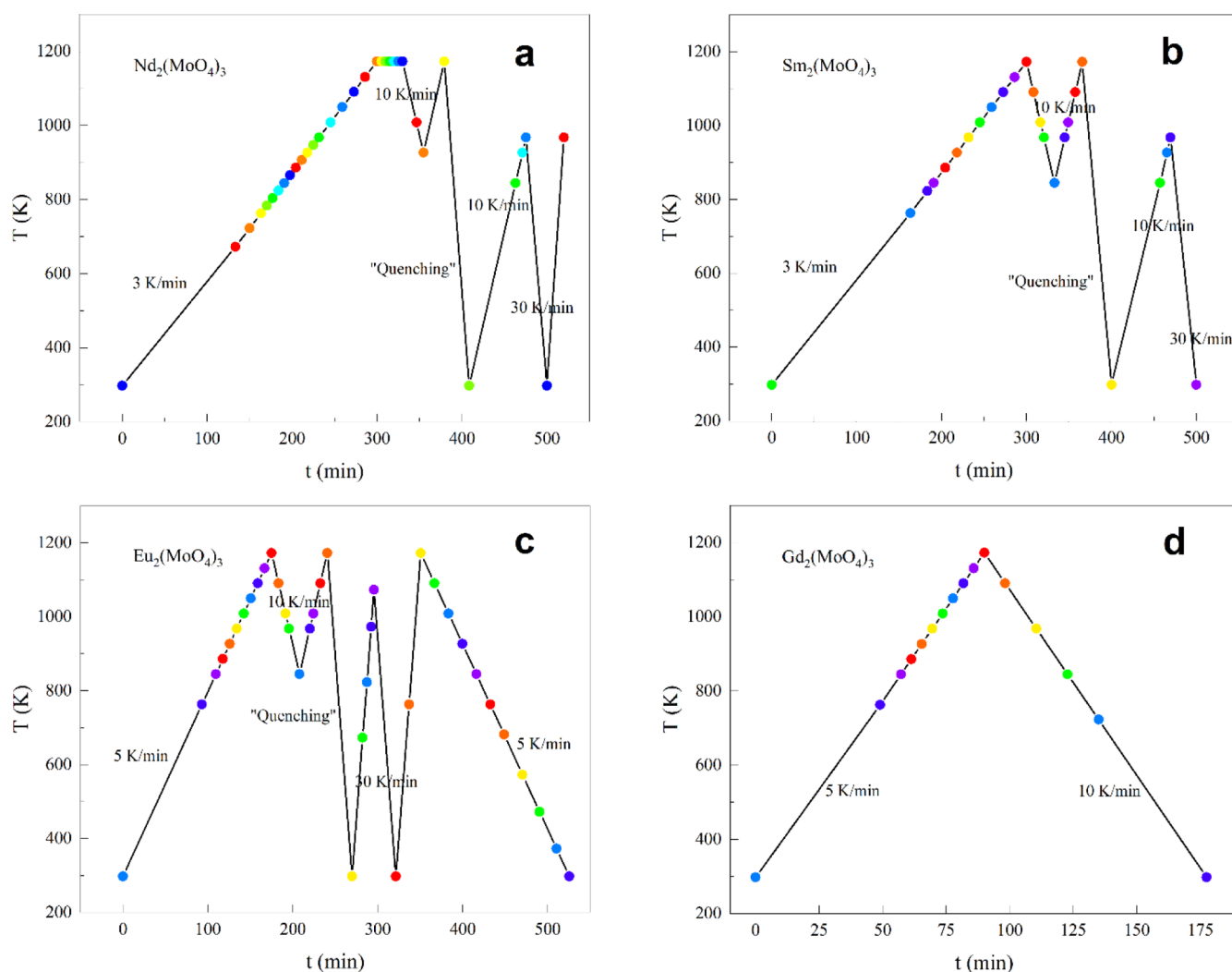
Figure 1. Heating–cooling cycles for $RE_2(MoO_4)_3$, RE ≡ (a) Nd, (b) Sm, (c) Eu, and (d) Gd.

other hand, depending on the ionic radius of the rare earth, there are several polymorphs with the formula $RE_2Mo_4O_{15}$ ($m/n = 1:4$), which have lately been studied for their optical properties.[37] In addition, the phase with the $Y_2Mo_4O_{15}$ structure undergoes NTE, increasing its functionality by doping or substituting with rare earth.[38,39] Other m/n compositions (1:5, 2:7, 3:10, etc.) are possible and have also been investigated.[40−42]

Despite many publications on the study of various characterization methods of lanthanide molybdates, investigating these physical and chemical properties and possible applications is still very relevant today. In particular, to understand in-depth the correlation between the physical properties and the crystal structure, it is necessary to know precisely and accurately the stability ranges of different phases as a function of temperature and the ionic radius of the rare earth. With this work, we aim to investigate the sequence and reversibility of the transitions between the paraelectric–ferroelectric ($\beta-\beta'$) phases and the α-phase or the LaMo-phase (modulated scheelite phases) in successive heating and cooling cycles. Moreover, the growth of such polymorphs, starting from the MoO_3 and RE_2O_3 oxides, has been studied because other non-stoichiometric molybdates are expected to appear, which would open new avenues of research. Four rare-earth molybdates with consecutive lanthanide elements in the

periodic table have been revised: $Nd_2(MoO_4)_3$, $Sm_2(MoO_4)_3$, $Eu_2(MoO_4)_3$, and $Gd_2(MoO_4)_3$ (Pm, between Nd and Sm, is radioactive, and the corresponding molybdate has been left out of this study for this reason). Note that compounds with lanthanides of immediately higher and lower ionic radii (Pr and Tb) are generally not synthesized from oxides with the formula RE_2O_3 and are not studied here. Data obtained in a thermodiffraction experiment performed at the ESRF (European Synchrotron Radiation Facility) in 2015 has been used for the present work. We have now analyzed and interpreted our results after reviewing new research on the different structural types occurring in most of the known rare earth molybdates.

2. EXPERIMENTAL SECTION

This work has been performed thanks to the European Synchrotron Radiation Facility (Grenoble, France) experiment with reference number ESRF: 25-01-954. The initial samples of the investigation were MoO_3 and RE_2O_3 oxides (RE: Nd, Sm, Eu, and Gd), previously preheated, mixed in stoichiometric quantities, and homogenized in an agate mortar. They were introduced into glass capillaries to complete the solid-state reaction during the thermodiffraction. Most of the experiments in the proposal were successfully performed, although time constraints did not allow the completion of some scheduled heating and cooling cycles. However, sufficient measurements were carried out to obtain new results, which explain the current

controversy on the formation and stability of this family of compounds.

2.1. Experimental Conditions of the Thermodiffraction. The measurements were taken for five consecutive days on the BM25A line. After establishing the experimental conditions referring to the standard samples, the experimental procedure consisted of heating up to 1273 K to get the desired phases synthesized, followed by a cooling and several subsequent heating and cooling cycles to determine the complete sequence of phase transitions. In general, in all these types of experiments, it is essential to maximize the number of diffractograms carried out at different temperatures but with sufficient time to measure each one.

Among the experimental conditions, the most relevant ones are pointed up. Quartz glass capillaries of 0.3 mm diameter were filled with the standard polycrystalline Si as a reference and the MoO_3, RE_2O_3 oxides, and different previously synthesized trimolybdate $RE_2(MoO_4)_3$ phases. The incident wavelength used was 0.6502 Å, obtained by checking the calibrated values concerning the interplanar spacings of the standard sample. The Debye–Scherrer geometry was used with a 2θ angular range from 4 to 15° or 30°. A hot gas blower was used for heating. The temperature was calibrated using the tabulated expansion curves of the Si sample from 298 to 1273 K. For this purpose, the Si sample was heated, and the peak data (111) were collected between 2θ = 11.8 and 12.0° in steps of 100 K in one heating cycle. Heating and cooling rates between 3 and 30 K/min were programmed for the remaining samples.

2.2. Heating and Cooling Programs. Figure 1 shows different heating and cooling schedules for the samples studied. Different molybdate phases were formed during the first heating cycle up to 1173 K. Many diffractograms were collected for the case of the first heating ramp. The first slow heating (3 K/min) to obtain the $Nd_2(MoO_4)_3$ and $Sm_2(MoO_4)_3$ molybdates was very similar since the aim was to compare the behavior of two different modulated scheelites before reaching the β-phase at 1173 K. Then, measurements were collected from 1173 to 873 K (at 10 K/min), and the temperature was raised again to 1173 K (10 K/min). This cycle was intended to study the reversibility of the α[LaMo]-β phase transitions. Afterward, the temperature was lowered by quenching to "freeze" the β'-phase, which was reheated (10 K/min) to observe the much less studied β–α[LaMo] change. Finally, the two samples were cooled down again quickly (30 K/min). During the first part of heating $Nd_2(MoO_4)_3$, the incidence of the hot gas did not heat the capillary homogeneously so that new phases were formed coexisting with the oxides, and it was maintained up to 1173 K. Several diffractograms were collected at this temperature while increasing the diameter of the gas flow. For this compound, final rapid heating from the β'-phase was also performed.

Molybdates of Eu and Gd were initially heated at 5 K/min. In the case of the $Eu_2(MoO_4)_3$ sample, the diffractograms were collected following the cycle RT-1173 K–873 K–1173 K (at 10 K/min), where the α–β–α–β phase transitions are expected. Then, a first rapid quenching to room temperature (30 K/min) was performed, and after that, the sample was heated to 1073 K at 30 K/min. This was followed by a new quenching to room temperature and a new heating until 1173 K (30 K/min). Finally, the sample was cooled at 5 K/min to collect more information about what happens when the temperature drops, since this part of the cycle is usually less studied. In the case of the $Gd_2(MoO_4)_3$ sample, the last compound analyzed, it was only possible to program a heating ramp at 5 K/min until reaching 1173 K, afterward a decrease at twice the rate, and collecting half the number of measurements.

2.3. Data Analysis. To identify the phases that appeared in the thermo-diffractogram, we performed an exhaustive search in the ICSD database (inorganic crystal structure database)[43] for the possible phases that could be present. Table 1 shows the most frequent structural types of the RE_2O_3 and MoO_3 oxides. Table 2 shows the structural types of the most frequent molybdates, where only the three elements, RE, O, and Mo(VI), appeared within the chemical formula and those where $\frac{2m}{n} \leq 0.\hat{6}$, where $2m$ is the number of rare earth and

Table 1. Different Structural Types of Rare Earth Oxides (RE: Nd, Sm, Eu, and Gd)

structural type	space group	Z	lattice parameters	rare earth
La_2O_3	$P\bar{3}m1$	1	a = 3.9 Å, c = 6.1 Å	La–Gd
$FeMnO_3$	$Ia\bar{3}$	16	a = 11.0 Å	Ce–Ho
Sm_2O_3	$C2/m$	6	a = 14.2 Å, b = 3.6 Å, c = 8.8 Å, β = 100°	Sm–Ho
MoO_3	$Pbnm$	4	a = 4.0 Å, b = 13.8 Å, c = 3.7 Å	

Table 2. Different Structural Types of Rare Earth Molybdates (RE: Nd, Sm, Eu, and Gd) with Different Stoichiometries

structural type	space group	Z	lattice parameters	rare earth
$CaWO_4$	$I4_1/a$	4	a = 5.3 Å, b = 5.3 Å, c = 11.9 Å	La–Eu
β-$Gd_2(MoO_4)_3$	$P\bar{4}2_1m$	2	a = 7.4 Å, b = 7.4 Å, c = 10.0 Å	Pr–Ho
β'-$Gd_2(MoO_4)_3$	$Pba2$	4	a = 10.0 Å, b = 10.4 Å, c = 10.0 Å	Pr–Ho
α-$Eu_2(WO_4)_3$	$C2/c$	4	a = 7.5 Å, b = 11.4 Å, c = 11.6 Å, β = 106°	Sm–Dy
$La_2(MoO_4)_3$	$C2/c$	12	a = 17.0 Å, b = 11.9 Å, c = 16.0 Å, β = 108°	La–Nd
$La_2Mo_4O_{15}$	$P2_1/n$	4	a = 9.0 Å, b = 12.7 Å, c = 10.6 Å, β = 90.2°	La
$La_2Mo_4O_{15}$	$P2_1/a$	12	a = 13.9 Å, b = 13.1 Å, c = 20.0 Å, β = 95.1°	La
$Pr_2Mo_4O_{15}$	$P\bar{1}$	2	a = 7.4 Å, b = 7.5 Å, c = 11.8 Å, α = 89°, β = 97°, γ = 95°	Ce–Nd
$Eu_2Mo_4O_{15}$	$P\bar{1}$	1	a = 9.4 Å, b = 10.5 Å, c = 11.5 Å, α = 104°, β = 110°, γ = 109°	Nd–Gd
$Eu_2Mo_5O_{18}$	$Pbcn$		a = 19.3 Å, b = 9.5 Å, c = 9.3 Å	Eu, Gd
$La_4Mo_7O_{27}$	$Pca2_1$	4	a = 14.1 Å, b = 7.3 Å, c = 23 Å	La
$Eu_4Mo_7O_{27}$	$C2/c$	4	a = 23.0 Å, b = 14.7 Å, c = 14.3 Å, β = 105°	Eu, Gd
$La_6Mo_8O_{33}$	$P2_1$	2	a = 10.7 Å, b = 12.0 Å, c = 11.7 Å, β = 116°	La
$Ce_5(MoO_4)_8$	$P2_1/c$	4	a = 11.3 Å, b = 17.0 Å, c = 14.0 Å, β = 90.7°	Ce
$Ce_6(MoO_4)_8(Mo_2O_{27})$	$P\bar{1}$	2	a = 9.4 Å, b = 10.6 Å, c = 18.1 Å, α = 104°, β = 95°, γ = 102°	Ce, Pr
$Nd_6Mo_{10}O_{39}$	$C2/c$	4	a = 12.4 Å, b = 19.8 Å, c = 13.8 Å, β = 101°	Pr–Gd

n is the number of molybdenum atoms. This condition implies that the chosen molybdates can co-exist with both oxides and only with the rare earth oxide when the molybdenum oxide has volatilized, taking into account that the ratio of the starting oxides must be m/n = 1:3 to obtain a mixture of phases with the total chemical formula: $RE_2Mo_3O_{12}$. Note that very stable compounds are not formed for lower m/n ratios. For instance, compounds with the 1:6, 1:7, 1:8, etc.,

ratios were not found in the database. The simulation of the theoretical diffractograms for phase identification was performed with the FullProf software.[44] Tables 1 and 2 also show the space group of each structural type, the number of chemical formula units in the unit cell, approximate lattice parameters, and the rare earth most frequently involved in these structural types.

To confirm all the identified phases, they were refined. Because of the small angular range of diffraction measurements, there was insufficient information to perform a Rietveld refinement;[45] thus, the Le Bail method was used to refine the complete profile.[46] We started the first refinement from the cell parameters used in the identification. Several points were chosen from the diffractogram to model the background, and a linear interpolation was performed. The modified Thompson−Cox−Hastings' pseudo-Voigt function was selected as the profile function, which involves asymmetry corrections for axial divergence.[47] The diffraction experiment was performed with the standard Si sample to obtain the starting profile parameters. The parameters U and X (associated with the micro deformations and domain or grain size, respectively) were refined, imposing the same value for all the phases refined in the same diffractogram. Other, more specific data treatments will be explained in the discussion of the results.

3. RESULTS AND DISCUSSION

Figure S1 shows the diffractograms collected during the first heating cycle. At room temperature, molybdenum oxide and oxides of Gd, Eu, Sm, and Nd were identified. Above 763 K, new peaks appear, which co-exist with the oxides and have been identified as "non-stoichiometric or intermediate molybdates" (see Table 2). At 886 K, the α-phase was identified for $Eu_2(MoO_4)_3$ and $Gd_2(MoO_4)_3$ and at 927 K for $Sm_2(MoO_4)_3$ and $Nd_2(MoO_4)_3$. In this first heating cycle, the solid-state reaction takes place, leading to the formation of the α-phase, which reaches its pure state at the temperature of 1050 K for Eu and Gd molybdates and at 1091 K for the Sm molybdate. The diffractograms of the Nd molybdate were more difficult to analyze because this compound was not uniformly heated, as explained in the Supporting Information.

The temperature of appearance of the modulated scheelites is lower when the lanthanide radius is smaller. The β-phase appears at 1091 K in Eu and Gd molybdates and at 1131 K in Nd and Sm molybdates. Also, it is found that this phase occurs at lower temperatures in compounds with lanthanides of a smaller ionic radius.

The following cooling and heating cycles are shown in Figures S2 and S3 at the Supporting Information where the phase transitions $\alpha \rightleftarrows \beta$ and LaMo $\rightleftarrows \beta$ were identified. A refinement of the complete profile was performed by the Le Bail method to go deeper into the formation and phase transitions and their mechanisms. In the following sections, we will discuss the results of these refinements, taking into account the crystal structures of the phases present. We will differentiate between the first heating cycle, the remainder cycles, and the specific treatment of $Nd_2(MoO_4)_3$.

3.1. First Heating Cycle: Molybdate Formation. In Figures 2−4 we show selected diffractogram refinements for the first heating cycle of the Gd, Sm, and Nd molybdates. (Similar refinements for the Eu molybdate diffractograms are shown in the Supporting Information in Figure S4). Experimentally obtained diffractograms (red) and those calculated theoretically by the Le Bail's method (black) are distinguished. In addition, the Bragg reflections of the different phases are shown. For all compounds, very similar results are observed, confirming the occurrence of non-stoichiometric (or intermediate) molybdates with type structures $Eu_4Mo_7O_{27}$ in
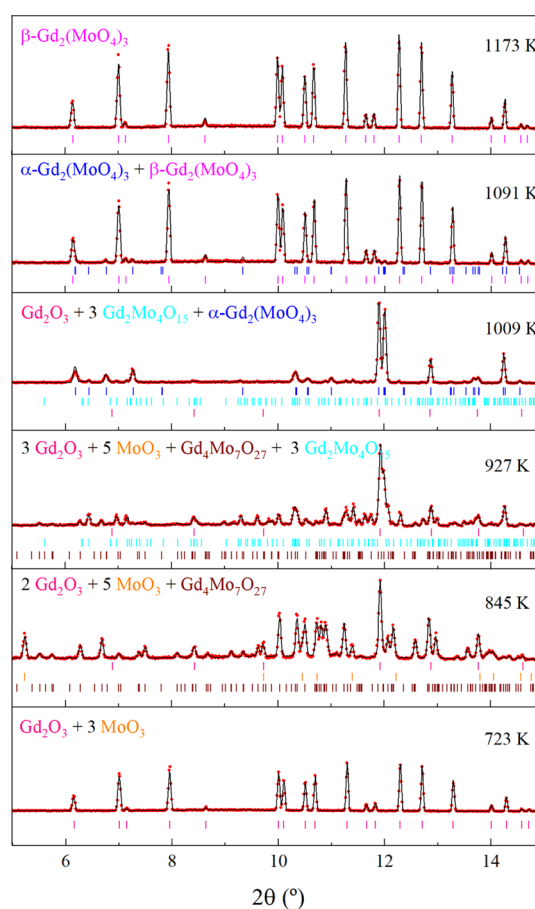

Figure 2. Le Bail refinements at different temperatures for $Gd_2(MoO_4)_3$. Observed data (red) and calculated data (black) are indicated. In addition, the Bragg positions for each of the phases: Gd_2O_3 (pink), MoO_3 (orange), $Gd_2Mo_4O_{15}$ (cyan), $Gd_4Mo_7O_{27}$ (brown), α-$Gd_2(MoO_4)_3$ (blue), and β-$Gd_2(MoO_4)_3$ (magenta) are indicated in the diffractograms.

all samples (marked as $RE_4Mo_7O_{27}$), $Pr_2Mo_4O_{15}$ in compounds with Nd (marked as $Nd_2Mo_4O_{15}$ (I)) and $Eu_2Mo_4O_{15}$ in molybdates with all rare earths (marked as $RE_2Mo_4O_{15}$). The first structural type co-exists with the MoO_3 oxide, and all of them with the corresponding rare earth oxides of the La_2O_3 structural types in compounds with Nd (marked as RE_2O_3 (I)) and of the $(MnFe)O_3$ structural type in the remaining compounds (marked as RE_2O_3).

The refinement confirmed the identified phases and that new unknown phases were not formed. Tables S1−S4 in the Supporting Information summarize the cell parameters and the agreement factors of each phase refinement (R_B and R_F) and for the complete profile (R_p, R_{wp}, R_{exp}, and χ^2) at different temperatures for each sample. In general, a good agreement was observed. However, the R_B and R_F factors of the compounds with Nd are worse due to the difficulty of refining all the phases coexisting for some temperatures during the first inhomogeneous heating. Sometimes the refinement of the pure oxide mixture was not satisfactory (large χ^2 values) because the profile model did not have all the parameters to fit the well-defined peaks.

The refinement also allows for an analysis of the unit cell volumes of different phases and their temperature dependence. The volume per atom within the unit cell was calculated to check the stability of the phases. All mixtures of phases must
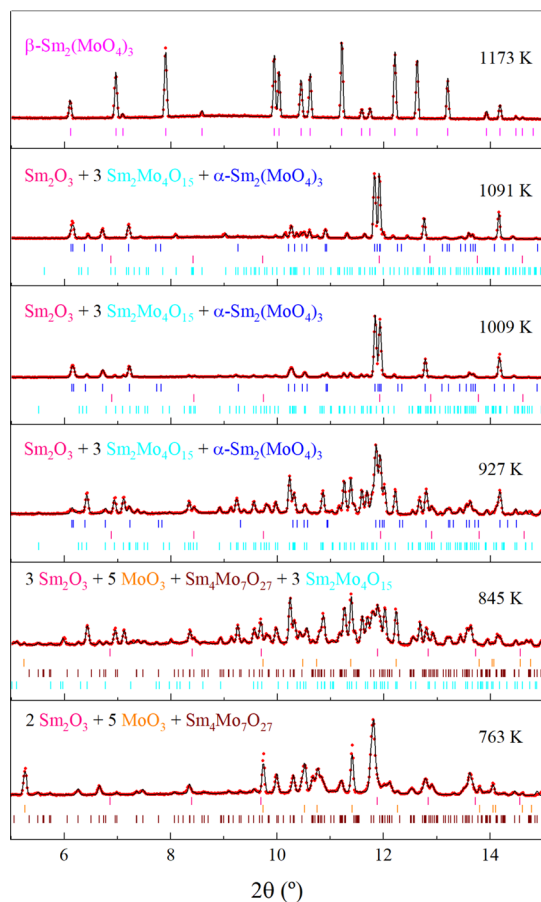
Figure 3. Le Bail refinements at different temperatures for $Sm_2(MoO_4)_3$. Observed data (red) and calculated data (black) are indicated. In addition, the Bragg positions for each of the phases: Sm_2O_3 (pink), MoO_3 (orange), $Sm_2Mo_4O_{15}$ (cyan), $Sm_4Mo_7O_{27}$ (brown), α-$Sm_2(MoO_4)_3$ (blue), and β-$Sm_2(MoO_4)_3$ (magenta) are indicated in the diffractograms.

Figure 4. Le Bail refinements at different temperatures for $Nd_2(MoO_4)_3$. Observed data (red) and calculated data (black) are indicated. In addition, the Bragg positions for each of the phases: Nd_2O_3 (I) (pink), MoO_3 (orange), $Nd_2Mo_4O_{15}$ (I) (cyan), $Nd_4Mo_7O_{27}$ (brown), β-$Nd_2(MoO_4)_3$ (magenta), and LaMo-$Nd_2(MoO_4)_3$ (green) are indicated in the diffractograms.

have the same number of atoms (we will call them: n_{RE}, n_{Mo}, and n_O), with $n_{RE} = 2\,N$, $n_{Mo} = 3\,N$, and $n_O = 12\,N$. Figure 5 shows the cell volumes per atom of the different phases appearing in the first heating cycle for the Nd, Sm, Eu, and Gd molybdates calculated during the refinement (in some cases completed with data collected in other cycles). The sums of the volumes of the stoichiometric mixture of lanthanide oxides and Mo oxides are the smallest and increase with the RE (Sm, Eu, and Gd) ionic radius. Note that this sum is lower for the Nd compound because it starts from Nd_2O_3, with another structural type denser than the other lanthanide oxides. This oxide is present at higher temperatures because heating was not uniform for neodymium compounds. The volumes per atom of the LaMo- and the α-phase are intermediate between the oxide mixtures and the β- and β'-phases, which present the larger volume per atom; this is typical for the metastable phase at a higher temperature. The volumes per atom of the intermediate molybdates are always between the volumes per atom of the $\alpha[LaMo]$ and β-phases after the temperature of the first appearance of the $\alpha[LaMo]$-phase and the $\alpha[LaMo]$ $\leftrightarrow \beta$ phase transition. Before this temperature, the mixtures of intermediate phases have a volume per atom close to that of the α-phase. In general, the volumes increase with the ionic radii of the lanthanide, and as the temperature increases, the volume increases unless a phase transition occurs; there may
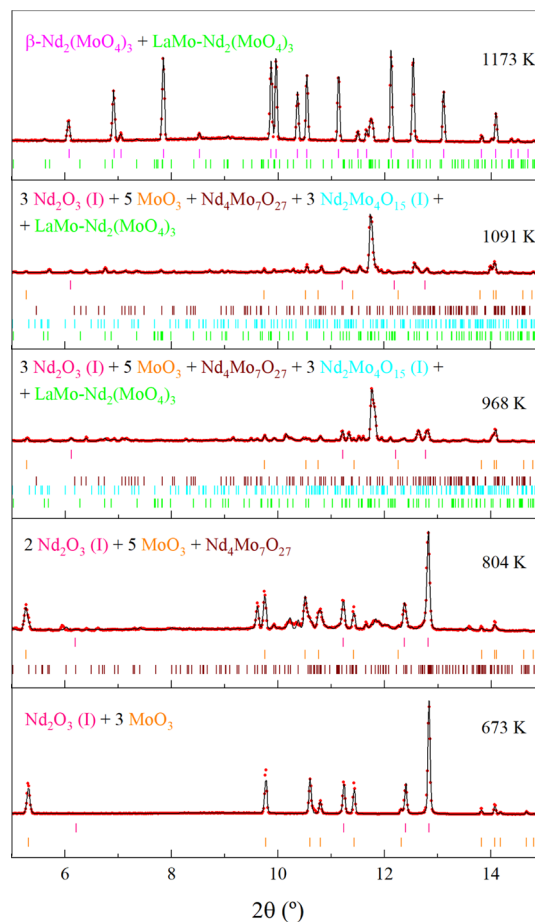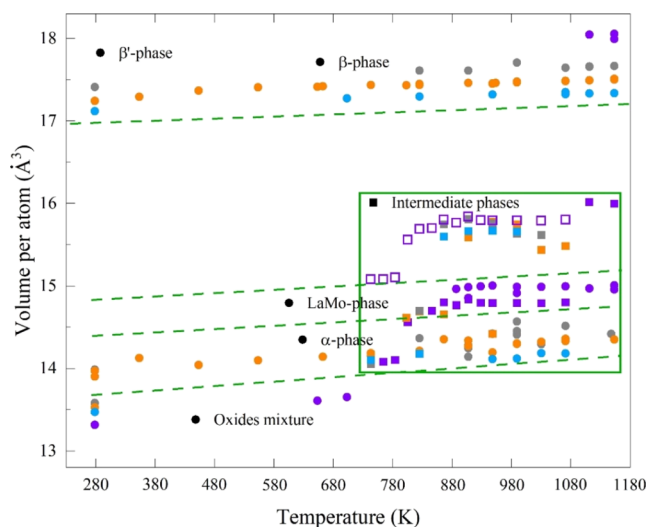

Figure 5. Volume per atom during the formation of the α, β, and β' phases starting from oxides.

be a decrease in volume and then a sharp increase with phase change. This process is less evident in forming $Nd_2(MoO_4)_3$; the calculated volumes do not correspond to a single

temperature because the sample was not uniformly heated during the first cycle. In Figure 5, we have estimated the volume per atom that Nd compounds should have (empty squares).

It is possible to describe the structures of the molybdates being formed in the first heating cycle (Figure 6) by attending
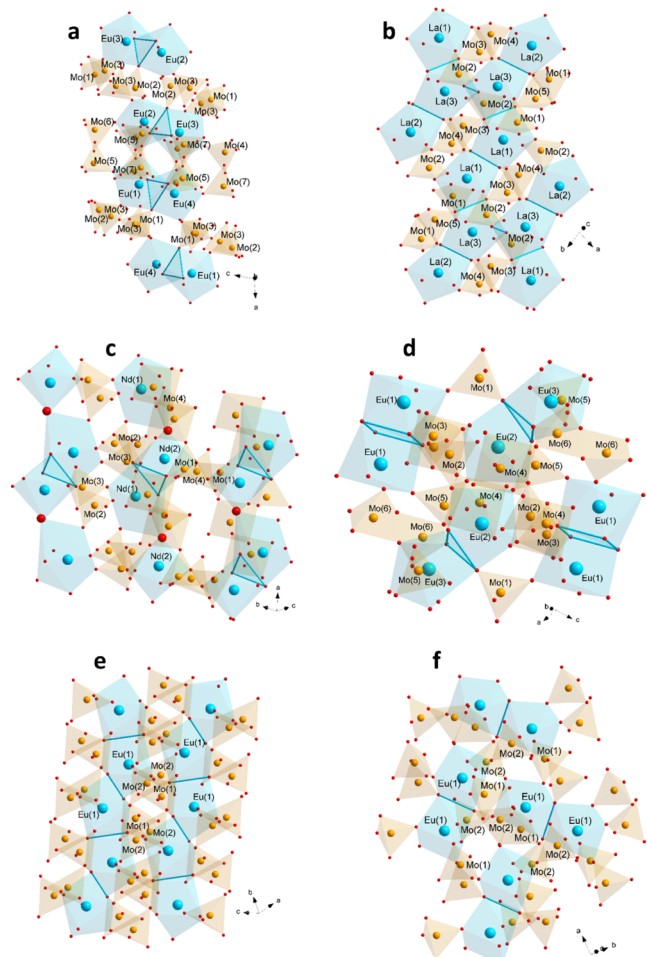

Figure 6. View of the molybdates (a) $Eu_4Mo_7O_{27}$, (b) $La_2(MoO_4)_3$, (c) $Pr_2Mo_4O_{15}$, (d) $Eu_2Mo_4O_{15}$, (e) α-$Eu_2(WO_4)_3$, and (f) β-$Gd_2(MoO_4)_3$ phases to show lanthanide dimers and bands.

to structural aspects similar to their precursor oxides $m_{Ln_2O_3}$–n_{MoO_3}, as proposed by Bandurkin and co-authors.[48] The structures of rare-earth molybdates inherit infinite dimer bands $\{[LnO_n]-[LnO_n]\}$ from the Ln_2O_3 oxides. The nanostructural "memory" of molybdates implies that the dimers of these bands retain approximately nanometer sizes and a predominant mutual orientation. This is possible even though, as the Mo content increases, the shape of the polyhedra in the dimers changes and the contacts between them and the forming polyhedra are eventually lost. The mentioned authors found that for the molybdate crystal structures, with oxide compositions n/m = 1:1, 1:3, and 1:4, the infinite bands of polyhedra building the cationic sublattice in the oxide are transformed into four modified endless band types:

(I) ...–$\{[LnO_n]-[LnO_n]\}$–$\{[LnO_n]-[LnO_n]\}$–..., (n = 8, Ln–Ln 3.7–4.0 Å). Example: α-$Eu_2(WO_4)_3$ (1:3), Figure 6e.

(II) ...$\{[LnO_n]\Delta[LnO_n]\}\cdot\{[LnO_n]\Delta[LnO_n]\}$..., ($n$ = 8, Ln–Ln ~ 3.9 Å). Example: $Pr_2Mo_4O_{15}$ (1:4), Figure 6c.

(III) ...$\{[LnO_n]-[LnO_n]\}$, $\{[LnO_n]-[LnO_n]\}$..., (n = 7, Ln–Ln ~ 4.0–4.5 Å); Examples: β-$Gd_2(MoO_4)_3$ and β'-$Gd_2(MoO_4)_3$ (1:3), Figure 6f.

(IV) ...$\{[LnO_n], [LnO_n]\}$, $\{[LnO_n], [LnO_n]\}$..., (n = 6,7, Ln–Ln ≥ 5.22 Å). Example: $Y_2Mo_4O_{15}$ (1:4), γ-$Sc_2(WO_4)_3$.

When the polyhedra share faces, we write a delta "Δ" or a square "$\square$"; when they share edges, a straight line "−"; and when they share vertices, a point "·". Three more groups can be added to incorporate the structures that do not belong to any of the previous groups:

(I′) −$\{6$-$[LnO_n]\}$−$\{6$-$[LnO_n]\}$−, (n = 8, Ln–Ln 3.7–4.0 Å). Example: $La_2(MoO_4)_3$ (1:3), Figure 6b.

(II′) ... $\{[LnO_n]\Delta[LnO_n]\}$, $\{[LnO_n]\Delta[LnO_n]\}$..., (n = 8, Ln–Ln ~ 3.9 Å). Example: $Eu_4Mo_7O_{27}$ (2:7), Figure 6a.

(II″) ...$\{[LnO_n]\Delta[LnO_n]\}$, $\{[LnO_n]\square[LnO_n]\}$..., ($n$ = 8, Ln–Ln ~ 3.9 Å). Example: $Eu_2Mo_4O_{15}$ (1:4), Figure 6d.

Thus, the sequence of intermediate molybdate structures can be explained. As the composition of the m/n oxides and the ionic radius of the lanthanide change, the bands of polyhedra $[LnO_n]$ in isolation or forming differently connected dimers are broken or rejoined. The first molybdates of the $Eu_4Mo_7O_{27}$ type (group II′) are created by co-existing with molybdenum and rare earth oxides, regardless of the lanthanide ionic radius. Then, the molybdenum oxide is volatilized, and molybdates $Pr_2Mo_4O_{15}$ (group II) and $Eu_2Mo_4O_{15}$ (group II″) are formed, depending on the lanthanide's radius. They still keep the dimers sharing faces, although the larger polyhedra allow the dimers to form infinite chains connecting through the vertices. At higher temperatures, modulated scheelites are formed: the α-phase (group I) and the LaMo-phase (group I′). They also differ according to the lanthanide radius. All polyhedra share an edge, forming infinite chains staggered every two dimers (α-phase) and hexamers connected by edges in a staggered manner (LaMo-phase). These are more compact structures than the previous ones as the proportion of lanthanide polyhedra increases. The temperature increase breaks the chains, favoring the isolated dimers sharing edges again, and the polyhedra decrease their coordination (n = 7); the β-phase (group III) has formed.

3.2. Next Cooling and Heating Cycles. All diffractograms obtained in subsequent cooling and heating cycles of the different samples were also refined. The agreement factors were generally better than the diffractograms of the first heating because never more than two phases co-existed (see Tables S5–S8 from the Supporting Information). Also, the R_B and R_F factors are always worse for minority phases. The profile factors (R_p, R_{wp}, χ^2) increase slightly when we have very well-defined peaks due to the lack of parameters modeling the profile.

Figure 7 shows five diffractograms of the compounds one can view at different temperatures and gives an idea of the quality of the refinements. From top to bottom: the β- (at 723 K) and β'- (room temperature) phases of $Gd_2(MoO_4)_3$ upon cooling, the coexistence of the α- and β'- phases in $Eu_2(MoO_4)_3$ at room temperature (last cooling), of the α- and β-phases in $Sm_2(MoO_4)_3$ at 927 K at the last heating, and finally the α-phase of $Sm_2(MoO_4)_3$ at room temperature at the last cooling.

Therefore, the $\beta'-\beta-\alpha-\beta$ transitions in Eu and Sm molybdates are confirmed. The cooling rate must be lower
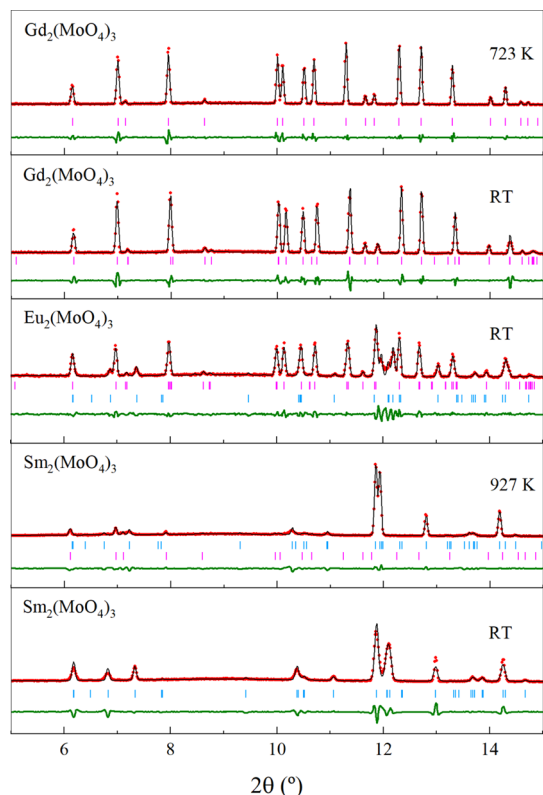
Figure 7. From top to bottom, $Gd_2(MoO_4)_3$ refinements at 723 K and room temperature. $Eu_2(MoO_4)_3$ refinement at room temperature and $Sm_2(MoO_4)_3$ refinements at 927 K and room temperature. Observed data (red), calculated data (black), and the difference between them (olive) are indicated. Bragg positions for the α-$Eu_2(WO_4)_3$ (sky blue) and β-$Gd_2(MoO_4)_3$ phase (magenta) also are indicated.

in Eu molybdate than in Sm molybdate to achieve the α-phase. In Gd molybdate, the cooling rate should have been slower to achieve the α-phase upon cooling. The ferroelectric and paraelectric phases are more stable for smaller lanthanide ionic radii, as Nassau and co-workers proposed.[31] However, the γ−β transition proposed for $Tb_2(MoO_4)_3$ upon cooling was never observed. The exothermic peak observed by these authors upon heating must correspond to the β−α transition. Furthermore, our experiments corroborate that the last two phases detected by Tang and co-workers[33] are the modulated α or LaMo scheelite rather than a new modulated scheelite. The formation of the scheelite phase at lower temperatures has not been observed. It should be noted that the diffractograms presented by these authors contain impurities (possibly "intermediate" oxides and other molybdates) that may lead to errors in identifying the modulated scheelites. Regarding the results of the DTA curves, we believe that the first exothermic peak above 873 K (which they assign to the modulated scheelite−scheelite transition) corresponds to the formation of the modulated scheelite phase (α- or LaMo-phase) from the non-stoichiometric (or intermediate) molybdates and rare earth oxides. We do agree with Tang et al.[33] that the second peak corresponds to the α−β transition.

There is a perfect correlation between the volume cell of the β-phase and the volume cell of the α-phase (see the Supporting Information, Figure S5). Note that in the case of $Nd_2(MoO_4)_3$ with the $La_2(MoO_4)_3$ structure-type, its volume V is divided by three since $V_{[La_2(MoO_4)_3]} \approx 3V_{[\alpha-Eu_2(WO_4)_3]}$. The increase in

volume of the β-phase with respect to the α-phase (plotted versus the ionic radii in Figure S5 in the Supporting Information) is around 20−22%, according to Morozov and co-authors.[18]

For a deeper analysis of the mechanisms for the reversible α−β and β−α transitions, the dependence on the temperature of the interplanar spacings of both phases can be plotted for all compounds (Figure S6 of the Supporting Information). There is no "collapse" of equivalent crystallographic directions in both phases, which confirms that it is a reconstructive (α−β or β−α) transition. The evolution of the β-phase spacings is very similar for all four compounds. When the temperature increases, the spacing increases in several crystallographic directions, decreases in others, and then reaches a normal increase. This behavior is expected in molybdates with modulated scheelite structures where the abnormal behavior of the a parameter [planes (200), (-202), (-113) etc.], is correlated with a polaronic conductivity in the same temperature range.[49] The abnormal behavior of the c parameter [plane (003)] in the β'-phase takes place before the transition to the β-phase, above 400 K.[50]

On the other hand, the $\alpha \rightarrow \beta$ phase transformation changes the coordination polyhedra for the rare-earth cations from LnO_8 to LnO_7. Unlike the α-phase with a scheelite-like structure, the β-$Gd_2(MoO_4)_3$ structure-type does not contain ...−{[LnO_8][LnO_8]}−{[LnO_8][LnO_8]}−... bands and lanthanide polyhedra form isolated dimers. To better understand the mechanisms leading to the α−β or β−α transitions, a first analysis has been performed, similar to the well-known $\alpha \rightarrow \beta$ reconstructive phase transitions of $LiNH_4SO_4$ crystals.[51,52] Figure 8 shows a view containing the b (α-phase) and c (β-
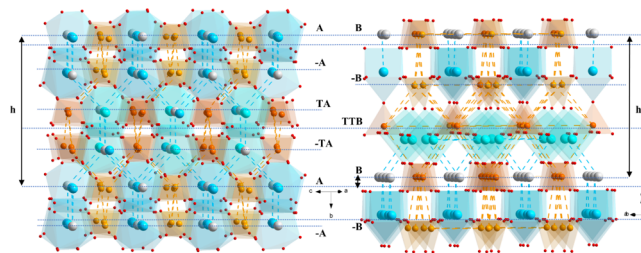

Figure 8. View of the α-phase (left) and β-phase (right) structures to visualize the sequence of rows along the b- and c-directions, respectively. We show the RE atoms in blue, the vacancies in gray, the Mo atoms in orange, and the oxygen atoms in red.

phase) axes along the vertical direction. We will call [A, -A, TA, -TA, A, and -A] the sequence of rows of tetrahedra of the α-phase (left) and [B, -B, TTB, B and -B] the series of rows of tetrahedra of the β-phase (right). Note that the sequence continues, and it is compatible with the lattice periodicity. Regarding the arrangement and orientation of the tetrahedra, rows A and B are very similar. Also, the arrangement of the tetrahedra at rows -A and -B is similar, but their orientation with respect to rows A (axis b) and B (axis c) is opposite. It is observed that rows B and -B are farther apart than rows A and -A. Rows TA and -TA have the tetrahedra translated in the direction horizontal from the figure and are mutually opposite; they are painted in dark orange. The row TTB, with translations along directions a and b of the tetrahedra from rows B and -B, is placed in the middle of the rows TA and -TA, changing the arrangement sequence (they are painted in dark orange). Moreover, within the same vertical length (h and h'),

there is one row less for the β-phase. To make the A and B rows coincide again, it is necessary to multiply by 3 the b parameter of the α-phase and by 4 the c parameter of the β- (or β'-) phase. It is also observed that the contacts between molybdates in rows A and -A and TA and -TA are similar to those in rows B and -B.

To explain what happens with the coordination polyhedra of lanthanides, we must take into account the position of the cation vacancies described by Aracheva in 2007[23] for modulated scheelites and by Morozov and co-workers (2014)[18] for the β- and β'-phases. In Figure 8, these positions are drawn as gray atoms. In the α-phase, the vacancies are placed at the same height as lanthanides. In the β-phase, the vacancies always belong to B-rows, and the lanthanides are placed slightly above the tetrahedra in the -B-rows and slightly below the TTB-rows. Figure 9 shows the planes perpendicular
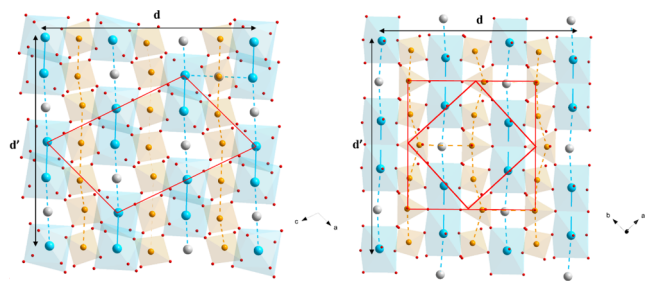

Figure 9. Projections of rows A and -A of α structure (left) and rows B and -B of β structure (right) in the b and c directions, respectively. The unit cells are drawn in red perpendicular to the b-axis (α-phase) and c-axis (β-phase), with the same color code as in Figure 8.

to axis b containing rows A and -A (α-phase) and the planes perpendicular to c forming rows B and -B (β-phase). Changes in the orientation of the β-phase from the α-phase are observed, and their connectivity is maintained by zig-zagging (orange dashed lines). The REO$_8$ polyhedra in the α-phase are connected two by two along the a-axis (vertical direction in Figure 9) by zig-zagging (blue dashed lines), and each pair is connected to a cation vacancy. Note that the polyhedra are not at the same height (along the vertical axis of Figure 8). In the β-phase, the contact of the lanthanides with the vacancy by zig-zagging (blue lines) in the vertical of Figure 9 persists. Still, the cations are at the same height, and the vacancy is at another height.

Figure 10 shows the planes perpendicular to b containing rows TA and -TA (α-phase) with connections of the vertical
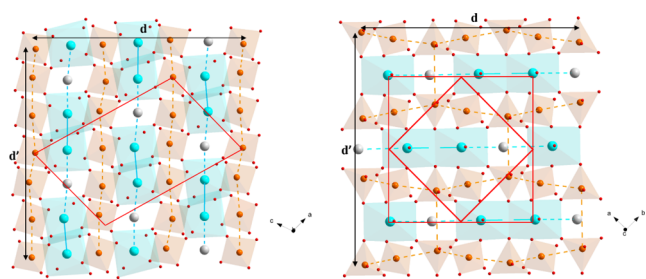

Figure 10. Projections of rows TA and -TA of the α structure (left) and rows TTB and B of the β structure (right) along the b and c directions, respectively. The unit cells are drawn in red perpendicular to the b-axis (α-phase) and c-axis (β-phase), with the same color code as in Figure 8.

polyhedra (similar to the planes in Figure 9), and the planes perpendicular to c containing rows TTB, but with connections of the horizontal polyhedra. This is related to the displacement of the tetrahedra of the row TTB along the direction of the diagonal of the ab plane. Each tetrahedron of the row B is diagonally connected with three tetrahedra of the row TTB. The vacancies of the β-phase remain in the same positions as in rows B and -B. This behavior is similar to that between rows -A with TA and -TA with A. The TTB and B rows of the β-phase are rotated 90° with respect to the TA and -TA rows of the α-phase (Figure 10). The most significant changes in the β-phase with respect to the α-phase are the formation of the row of TTB tetrahedra in the β-phase and the rearrangement of lanthanides and vacancies. A similar discussion can be had if we compare the β-phase with the LaMo-phase, considering that the ordering of vacancies and lanthanides is different.

It must be added that significant deformation and large atomic displacements are required in this phase transition, and there is no group relationship between the symmetries of the two crystalline phases. Any detailed description of a reconstructive phase transition must address two questions: (1) how do the atoms move from one structure to the other? And (2) what path do the atoms follow between these two structures?[53] From the comparisons made between the α- and β-phases, the first question concerning the mapping, i.e., how the two structures are related, is resolved. We have chosen a super-cell (a, b, and c) with the minimum symmetry belonging to a common monoclinic space subgroup ($P2$). Both structures would be related considering the following matrix equations between the parameters of the α-cell (a_α, b_α, and c_α) and the β-cell (a_β, b_β, and c_β).

$$\begin{pmatrix} a \\ b \\ c \end{pmatrix} = \begin{pmatrix} 2 & 0 & -2 \\ 0 & 3 & 0 \\ 2 & 0 & 4 \end{pmatrix} \begin{pmatrix} a_\alpha \\ b_\alpha \\ c_\alpha \end{pmatrix} = \begin{pmatrix} 3 & 3 & 0 \\ 0 & 0 & 4 \\ -3 & 3 & 0 \end{pmatrix} \begin{pmatrix} a_\beta \\ b_\beta \\ c_\beta \end{pmatrix}$$

We can also find the relationship of the LaMo-phase (of parameters a_{LaMo}, b_{LaMo}, and c_{LaMo}) to the β-phase.

$$\begin{pmatrix} a \\ b \\ c \end{pmatrix} = \begin{pmatrix} 2 & 0 & -2/9 \\ 0 & 3 & 0 \\ 0 & 0 & 2 \end{pmatrix} \begin{pmatrix} a_{LaMo} \\ b_{LaMo} \\ c_{LaMo} \end{pmatrix} = \begin{pmatrix} 3 & 3 & 0 \\ 0 & 0 & 4 \\ -3 & 3 & 0 \end{pmatrix} \begin{pmatrix} a_\beta \\ b_\beta \\ c_\beta \end{pmatrix}$$

Such supercells would have dimensions of approximately 30 × 30 × 40 Å. Referring to Figures 8−10: $a \approx 2d$, $b \approx 2d'$ ($d \approx d'$), and $c \approx 3h \approx 4h'$. The second question is more complicated to solve and has to do with the actual atomic displacements and stresses that occur during the phase transition, and we will not address it in this work.

3.3. Particular Heat Treatment for Nd$_2$(MoO$_4$)$_3$. Finally, we have to add that a phase mixture between the α-phase and the LaMo-phase was detected in the last heating cycle of the Nd$_2$(MoO$_4$)$_3$ compound at 968 K (Figure 11). Such a mixture was achieved by heating from room temperature the β'-phase at the rate of 30 K/min. It was expected to obtain the LaMo-phase, but peaks appeared that could be identified as the α-phase. However, the refinement did not yield good results as some peaks were not fitted. It could be an incommensurable phase similar to that of Pr$_2$(MoO$_4$)$_3$, which some authors described as stacking faults, interrupting the arrangement of cations and their vacancies.[24] If a modulation vector for the LaMo-phase is included in the refinement, the result improves,
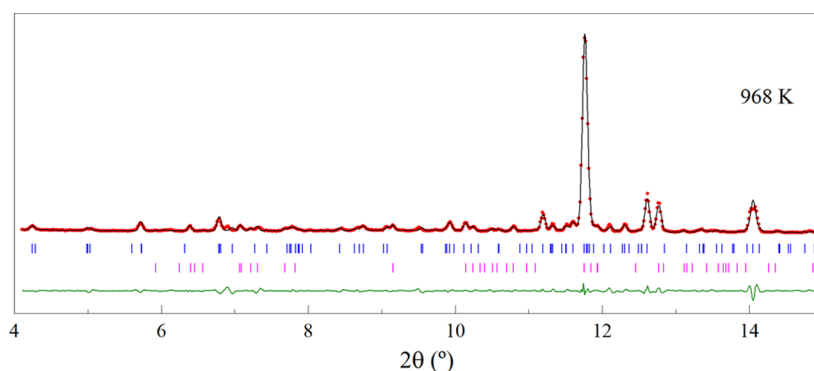
Figure 11. Diffractogram of $Nd_2(MoO_4)_3$ and refinement at 968 K. Experimentally observed data (red), calculated data (black), and the difference between them (olive) are indicated, in addition to the Bragg positions for the $La_2(MoO_4)_3$ phase (blue) and the $Eu_2(WO_4)_3$ phase (pink).

but the peaks associated with the α-phase are still not well refined. When a modulation vector for the α-phase was included, the refinement improved. Therefore, phase mixing may be compatible with the occurrence of two incommensurable phases in which the stacking faults are consistent with each co-existing phase.

Revisiting the results of Popov and co-workers,[20] we pay attention to the incommensurable phases they propose for the whole series of compounds with the formula $RE_2(MoO_4)_3$. These have modulation vectors in which the second component (along the $\boldsymbol{b}*$ direction) decreases as the radius of the lanthanide decreases. It can be explained as a continuous transition from the LaMo- to the α-phase, where the second component decreases from 8/9 to 2/3. Figure 12 shows the change in the vacancy (lanthanide cations) arrangement for the modulation vectors: (a) $\boldsymbol{q} = 2\boldsymbol{a}*/3 + 2\boldsymbol{b}*/3$, (b) $\boldsymbol{q} = 2\boldsymbol{a}*/3 + 0.7\boldsymbol{b}*$, (c) $\boldsymbol{q} = 2\boldsymbol{a}*/3 + 0.75\boldsymbol{b}*$, (d) $\boldsymbol{q} = 2\boldsymbol{a}*/3 + 0.8\boldsymbol{b}*$, (e) $\boldsymbol{q} = 2\boldsymbol{a}*/3 + 0.85\boldsymbol{b}*$, and (f) $\boldsymbol{q} = 2\boldsymbol{a}*/3 + 8\boldsymbol{b}*/9$. Starting from infinite bands of lanthanides and vacancies forming the α-phase (red blocks in Figure 12a), first stacking defects emerge, and the vacancy (or cations) bands are broken, forming clusters marked with dark orange rectangles (Figure 12b,c). The defects then increase by building shorter vacancy clusters (or cations, marked with orange rectangles, see Figure 12d) until reaching the $La_2(MoO_4)_3$ structure-type with several defects, where bands of three vacancies (or cations) joined two by two are located in a staggered manner (yellow blocks in Figure 12e,f). The shape of the connected lanthanide polyhedra bands in the diagonal direction of modulated scheelites was explained at the end of Section 3.1. The α-phase contains two lanthanide chains and one vacancy chain, and the structure of $La_2(MoO_4)_3$ combines staggered connected hexamers with staggered vacancy trimers (Figure 6). Popov and co-authors also found the incommensurable component along the other direction of the tetragonal scheelite (the $\boldsymbol{a}*$ direction) in the incommensurable phases.[20] This complicates the model, as new defects must appear along the other diagonal of the structure, which is more difficult to assume because, in this direction, neither lanthanide polyhedra nor vacancy-forming bands and clusters are connected. Therefore, it is more appropriate to model a mixture of the α- and LaMo-phases which, in turn, could be incommensurable only concerning the second component of the modulation vector. The formation of defects can be explained by very rapid heating from the more open β-phase, which undergoes the modulated scheelite mixture. These defects have also already been identified by applying pressure on the α-phase of the
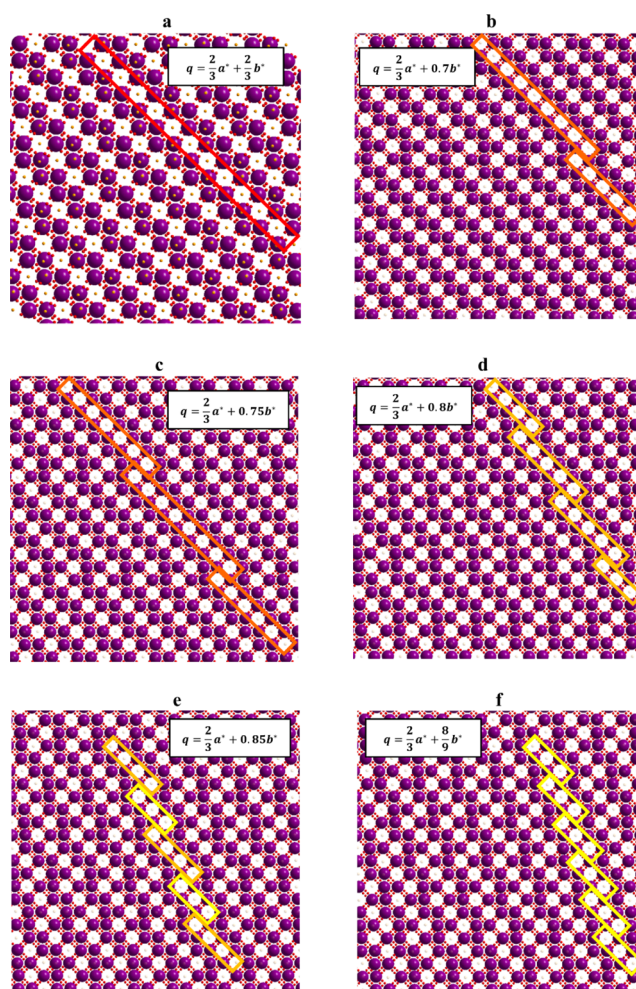

Figure 12. Projections along the $\boldsymbol{b}$ direction of different phases modulated with the superspace group $I112/\boldsymbol{b}$. Progressive increase of the $\boldsymbol{b}*$ component from (a) 0.6667 to (f) 0.8889 = 8/9, corresponding to the α- and LaMo-phases forming stacking faults. The vacancies are highlighted in red for the α-phase, with different shades of orange for the intermediate phases and yellow for the vacancy clusters for the LaMo-phase.

$RE_2(WO_4)_3$ tungstates.[54] However, further studies based on high-resolution transmission electron microscopy for the complete characterization of this family (as identified in similar series of dislocations, stacking faults, and modulated microstructures observed in the aragonite−calcite transition[55])

are needed. The formation of intermediate molybdates is less plausible once the compound with stoichiometry $RE_2(MoO_4)_3$ has been formed. Researchers should consider forming intermediate phases if they start from oxides or other precursors in their experiments.

4. CONCLUSIONS

This work presents an in situ study of the solid-state synthesis and phase transitions of four rare-earth molybdates with the formula $RE_2(MoO_4)_3$ (RE = Nd, Sm, Eu, and Gd). The synthesis was monitored by thermodiffraction using synchrotron radiation to assess the phases formation and transitions appearing in each of the heating and cooling cycles. The first significant achievement is the identification and refinement of the crystalline cell of all the phases and mixtures obtained.

During the first heating cycle, all compounds were formed with the stoichiometry of the proposed reaction, starting from the oxides: RE_2O_3 and MoO_3 with 1:3 compositions. Before 773 K, non-stoichiometric molybdates (also called "intermediates") were detected with $Eu_4Mo_7O_{27}$ and $Eu_2Mo_4O_{15}$ structures, mixed with the oxides in the diffractograms of all the compounds. In the case of the compounds with Nd, the $Pr_2Mo_4O_{15}$ structural type was also detected. The temperature at which the LaMo, α, and β phases appear and their dependence on the ionic radius were confirmed. The formation of all these phases is explained, especially the co-existence of the "intermediate" molybdates with the oxides and their stability as a function of temperature and ionic radius, taking into account: (1) the calculation of the volume per atom of all phases and mixtures where the starting stoichiometry is conserved, which was always larger than that corresponding to the oxide mixture and increased with temperature from the volume of the denser modulated scheelite-type phases to the more open β-phase. (2) The formation mechanisms of all these molybdates were proposed by studying common structural motifs, in particular the arrangement and connection of dimers formed by the lanthanide coordination polyhedra, depending on the ionic radii.

For subsequent heating and cooling cycles, the reversible $\alpha \leftrightarrow \beta$ and LaMo $\leftrightarrow \beta$ transitions and the dependence of the transition temperature on the ionic radius on the heating or cooling rate were confirmed. Very fast cool-downs (including quenching) did not allow the detection of the $\beta \rightarrow \alpha$ (or $\beta \rightarrow$ LaMo) transition. The $\beta \rightarrow \alpha$ and $\beta \rightarrow$ LaMo transitions were obtained by heating the β'-phase from room temperature. This ensured the complete reversibility of these reconstructive phase transitions. Identifying and refining these phases allowed us to determine their thermal stability ranges and clarified much of the controversy that sometimes appears in the very recent literature cited in this work. In addition, we have furthered the study of the reconstructive transition mechanisms by comparing the crystal structure of these phases. A common supercell for the α (or LaMo) and β phases was proposed, where the contacts between the MoO_4^{2-} tetrahedra are very similar. Turning to the positions of rare earth and vacancies is necessary to compare both structures.

Once the α-, LaMo-, or β-phases are formed, intermediate molybdates do not occur, even with further rapid cooling and heating cycles. However, mixtures of α- (or LaMo-) and β-phases and commensurable—incommensurable modulated scheelite phases were observed. The modulated phases have different wave vectors $q = 2a^*/3 + fb^*$ (2/3 < f < 8/9), depending on the ionic radius, and are associated with the

formation of defects produced by the rearrangement of lanthanides and their cationic vacancies during the thermal treatment.

Ultimately, for the continuous enrichment of materials with new or improved properties of technological interest, a directed and rational synthesis is needed, which requires the analysis of the intermediate compounds produced in solid-state synthesis and solid—solid phase transitions, which are sometimes very difficult to identify and isolate.

◼ ASSOCIATED CONTENT

Ⓢ Supporting Information

The Supporting Information is available free of charge at https://pubs.acs.org/doi/10.1021/acs.cgd.2c01387.

> Diffractograms (raw data) of the first warming and subsequent cooling—warming cycles performed in the $RE_2(MoO_4)_3$ compounds with RE = Nd, Sm, Eu, and Gd; tables of cell parameters and agreement factors for all the refined phases of the RE_2O_3 and MoO_3 oxides, the intermediate phases and the $RE_2(MoO_4)_3$ compounds; Le Bail refinements at different temperatures for $Eu_2(MoO_4)_3$; volume of the β-phase with respect to that of the α-phase and increase in the volume of the β-phase with respect to that of the α-phase plotted against the ionic radii; and interplanar spacings in the β and α crystal phases of $RE_2(MoO_4)_3$ compounds at different cooling—heating cycles (PDF)

◼ AUTHOR INFORMATION

Corresponding Author

Cristina González-Silgo − *Departamento de Física, Instituto Universitario de Materiales y Nanotecnología IMN, Universidad de La Laguna, San Cristóbal de La Laguna 38200 Santa Cruz de Tenerife, Spain;* ⓞ orcid.org/0000-0002-4731-3501; Email: csilgo@ull.edu.es

Authors

Ivan da Silva − *ISIS Facility, Science and Technology Facilities Council (STFC), Rutherford Appleton Laboratory, OX11 0QX Didcot, U.K.;* ⓞ orcid.org/0000-0002-4472-9675

Gerardo Gil de Cos − *Departamento de Física, Universidad de La Laguna, San Cristóbal de La Laguna 38200 Santa Cruz de Tenerife, Spain*

Javier López-Solano − *Izaña Atmospheric Research Center, Agencia Estatal de Meteorología AEMET, 38001 Santa Cruz de Tenerife, Spain;* ⓞ orcid.org/0000-0003-0127-4911

Andrés Mujica − *Departamento de Física, Instituto Universitario de Materiales y Nanotecnología IMN, MALTA Consolider Team, Universidad de La Laguna, La Laguna 38200 Tenerife, Spain*

Nivaria R. Ramírez-Rodríguez − *Departamento de Física, Universidad de La Laguna, San Cristóbal de La Laguna 38200 Santa Cruz de Tenerife, Spain*

Manuel E. Torres − *Departamento de Física, Instituto Universitario de Materiales y Nanotecnología IMN, Universidad de La Laguna, San Cristóbal de La Laguna 38200 Santa Cruz de Tenerife, Spain*

Complete contact information is available at:
https://pubs.acs.org/10.1021/acs.cgd.2c01387

Notes

The authors declare no competing financial interest.

■ REFERENCES

(1) Brixner, L. H.; Barkley, J. R.; Jeitschko, W. Rare earth molybdates (VI). *Handbook on the Physics and Chemistry of Rare Earths*; Elsevier, 1979; Vol. 3, pp 609-654.

(2) Nagornaya, L. L.; Danevich, F. A.; Dubovik, A. M.; Grinyov, B. V.; Henry, S.; Kapustyanyk, V.; Kraus, H.; Poda, D. V.; Kudovbenko, V. M.; Mikhailik, V. B.; Panasyuk, M.; Polischuk, O. G.; Rudyk, V.; Tupitsyna, I. A.; Vostretsov, Y. Y. Tungstate and molybdate scintillators to search for dark matter and double beta decay. *IEEE Trans. Nucl. Sci.* **2009**, *56*, 2513−2518.

(3) Zharikov, E. V.; Zaldo, C.; Díaz, F. Double tungstate and molybdate crystals for laser and nonlinear optical applications. *MRS Bull.* **2009**, *34*, 271−276.

(4) Wang, Z.; Liang, H.; Wang, J.; Gong, M.; Su, Q. Red-light-emitting diodes fabricated by near-ultraviolet InGaN chips with molybdate phosphors. *Appl. Phys. Lett.* **2006**, *89*, 071921.

(5) Fabbri, E.; Bi, L.; Pergolesi, D.; Traversa, E. Towards the Next Generation of Solid Oxide Fuel Cells Operating Below 600°C with Chemically Stable Proton-Conducting Electrolytes. *Adv. Mater.* **2012**, *24*, 195−208.

(6) Porotnikova, N.; Khrustov, A.; Farlenkov, A.; Khodimchuk, A.; Partin, G.; Animitsa, I.; Kochetova, N.; Pavlov, D.; Ananyev, M. Promising $La_2Mo_2O_9$−$La_2Mo_3O_{12}$ Composite Oxygen-Ionic Electrolytes: Interphase Phenomena. *ACS Appl. Mater. Interfaces* **2022**, *14*, 6180−6193.

(7) Xue, J. S.; Antonio, M. R.; Soderholm, L. Polymorphs of Ln_2MoO_6: A Neutron Diffraction Investigation of the Crystal Structures of La_2MoO_6 and Tb_2MoO_6. *Chem. Mater.* **1995**, *7*, 333−340.

(8) Colmont, M.; Boutinaud, P.; Latouche, C.; Massuyeau, F.; Huvé, M.; Zadoya, A.; Jobic, S. Origin of Luminescence in La_2MoO_6 and $La_2Mo_2O_9$ and Their Bi-Doped Variants. *Inorg. Chem.* **2020**, *59*, 3215−3220.

(9) Yang, H.; Zhang, S.; Yang, H.; Wen, Q.; Yang, Q.; Gui, L.; Zhao, Q.; Li, E. The latest process and challenges of microwave dielectric ceramics based on pseudo phase diagrams. *J. Adv. Ceram.* **2021**, *10*, 885−932.

(10) Orlova, E.; Kharitonova, E.; Sorokin, T.; Antipin, A.; Novikova, N.; Sorokina, N.; Voronkova, V. Structure and Properties of Ln_2MoO_6 Oxymolybdates (Ln = La, Pr, Nd) Doped with Magnesium. *Crystals* **2021**, *11*, 611.

(11) Arshad, H. M. U.; Liu, S.; Li, G.-R.; Gao, X.-P. La_2MoO_6 as an Effective Catalyst for the Cathode Reactions of Lithium−Sulfur Batteries. *ACS Appl. Mater. Interfaces* **2022**, *14*, 5247−5256.

(12) Orlova, E.; Chernyak, S.; Kharitonova, E.; Lyskov, N.; Sorokin, T.; Antipin, A.; Kvartalov, W.; Sorokina, N.; Voronkova, V. La_2MoO_6 Oxymolybdates Doped with Sodium: Crystal Growth, Features of the Structure, and Properties. *Cryst. Growth Des.* **2021**, *21*, 7043−7052.

(13) Guzmán-Afonso, C.; León-Luis, S. F.; Sans, J. A.; González-Silgo, C.; Rodríguez-Hernández, P.; Radescu, S.; Muñoz, A.; López-Solano, J.; Errandonea, E.; Manjón, F. J.; Rodríguez-Mendoza, U. R.; Lavín, V. Experimenyal and theoretical study of α-$Eu_2(MoO_4)_3$ under compression. *J. Phys.: Condens. Matter* **2015**, *27*, 465401.

(14) Brixner, L. H. Precision parameters of some $Ln_2(MoO_4)_3$-type rare earth molybdates. *Mater. Res. Bull.* **1971**, *6*, 545−554.

(15) Maczka, M.; Souza Filho, A. G.; Paraguassu, W.; Freire, P. T. C.; Mendes Filho, J.; Hanuza, J. Pressure-induced structural phase transitions and amorphization in selected molybdates and tungstates. *Prog. Mater. Sci.* **2012**, *57*, 1335−1381.

(16) Raju, G. S. R.; Pavitra, E.; Nagaraju, G. P.; Kandimalla, R.; El-Rayes, B. F.; Yu, J. S. PEGylated α-$Gd_2(MoO_4)_3$. Mesoporous Flowers: Synthesis, Characterization, and Biological Application. *Cryst. Growth Des.* **2013**, *13*, 4051−4058.

(17) Zou, H.; Chen, B.; Hu, Y.; Zhang, Q.; Wang, X.; Wang, F. Simultaneous Enhancement and Modulation of Upconversion by Thermal Stimulation in $Sc_2Mo_3O_{12}$ Crystals. *J. Phys. Chem. Lett.* **2020**, *11*, 3020−3024.

(18) Morozov, V. A.; Raskina, M. V.; Lazoryak, B. I.; Meert, K. W.; Korthout, K.; Smet, P. F.; Poelman, D.; Gauquelin, N.; Verbeeck, J.; Abakumov, A. M.; Hadermann, J. Crystal Structure and Luminescent Properties of $R_{2−x}Eu_x(MoO_4)_3$ (R= Gd, Sm) Red Phosphors. *Chem. Mater.* **2014**, *26*, 7124−7136.

(19) Huang, Q.; Xu, J. Z.; Li, W. Preparation of tetragonal defect scheelite-type $RE_2(MoO_4)_3$ (RE= La To Ho) by precipitation method. *Solid State Ionics* **1989**, *32-33*, 244−249.

(20) Popov, V. V.; Menushenkov, A. P.; Yastrebtsev, A. A.; Molokova, A. Y.; Rudakov, S. G.; Svetogorov, R. D.; Tsarenko, N. A.; Ponkratov, K. V.; Ognevskaya, N. V.; Seregina, O. N. The effect of the synthesis conditions on the structure and phase transitions in $Ln_2(MoO_4)_3$. *Solid State Sci.* **2021**, *112*, 106518.

(21) Jeitschko, W. Crystal structure of $La_2(MoO_4)_3$ a new ordered defect scheelite type. *Acta Crystallogr.* **1973**, *29*, 2074−2081.

(22) Templeton, D. H.; Zalkin, A. Crystal structure of europium tungstate. *Acta Crystallogr.* **1963**, *16*, 762−766.

(23) Arakcheeva, A.; Chapuis, G. Capabilities and limitations of a (3+d)-dimensional incommensurately modulated structure as a model for the derivation of an extended family of compounds: example of the scheelite-like structures. *Acta Crystallogr.* **2008**, *64*, 12−25.

(24) Logvinovich, D.; Arakcheeva, A.; Pattison, P.; Eliseeva, S.; Tomeš, P.; Marozau, I.; Chapuis, G. Crystal Structure and Optical and Magnetic Properties of $Pr_2(MoO4)_3$. *Inorg. Chem.* **2010**, *49*, 1587−1594.

(25) Sabalisck, N. P.; López-Solano, J.; Guzmán-Afonso, C.; Santamaría-Pérez, D.; González-Silgo, C.; Mujica, A.; Muñoz, A.; Rodríguez-Hernández, P.; Radescu, X.; Vendrell, L.; Mestres, J. A.; Sans, F. J.; Manjón, F. J. Effect of Pressure on $La_2(WO_4)_3$ with a Modulated Scheelite-Type Structure. *Phys. Rev. B: Condens. Matter Mater. Phys.* **2014**, *89*, 174112.

(26) Jeitschko, W. A Comprehensive X-Ray Study of the Ferroelectric−Ferroelastic and Paraelectric−Paraelastic Phases of $Gd_2(MoO_4)_3$. *Acta Crystallogr.* **1972**, *28*, 60−76.

(27) Borchardt, H. J.; Bierstedt, P. E. Ferroelectric rare-earth molybdates. *J. Appl. Phys.* **1967**, *38*, 2057−2060.

(28) Dmitriev, V.; Sinitsyn, V.; Dilanian, R.; Machon, D.; Kuznetsov, A.; Ponyatovsky, E.; Lucazeau, G.; Weber, H. P. In situ pressure-induced solid-state amorphization in $Sm_2(MoO_4)_3$, $Eu_2(MoO_4)_3$ and $Gd_2(MoO_4)_3$ crystals: chemical decomposition scenario. *J. Phys. Chem. Solids* **2003**, *64*, 307−312.

(29) Evans, J. S. O.; Mary, T. A.; Sleight, A. W. Negative thermal expansion in $Sc_2(WO_4)_3$. *J. Solid State Chem.* **1998**, *137*, 148−160.

(30) Shmurak, S. Z.; Kedrov, V. V.; Kiselev, A. P.; Fursova, T. N.; Zver'kova, I. I.; Khasanov, S. S. Spectral and Structural Characteristics of Molybdates $(Lu_{1−x}Eu_x)_2(MoO_4)_3$. *Phys. Solid State* **2019**, *61*, 632−641.

(31) Nassau, K.; Levinstein, H. J.; Loiacono, G. M. A comprehensive study of trivalent tungstates and molybdates of the type $L_2(MO_4)_3$. *J. Phys. Chem. Solid.* **1965**, *26*, 1805−1816.

(32) Atuchin, V. V.; Aleksandrovsky, A. S.; Chimitova, O. D.; Gavrilova, T. A.; Krylov, A. S.; Molokeev, M. S.; Oreshonkov, A. S.; Bazarov, B. G.; Bazarova, J. G. Synthesis and spectroscopic properties of monoclinic α-$Eu_2(MoO_4)_3$. *J. Phys. Chem. C* **2014**, *118*, 15404−15411.

(33) Tang, R. F.; Chen, H.; Yin, W. Y.; Li, Y. M.; Ning, Z. L.; Zhong, C.; Zhao, Y.; Lai, X.; Bi, J.; Gao, D. J. Temperature-induced phase transition, luminescence and magnetic properties of $Eu_2(MoO_4)_3$

microcrystal red phosphors. *J. Mater. Sci. Mater. Electron.* **2019**, *30*, 7347−7358.

(34) Goutenoire, F.; Isnard, O.; Retoux, R.; Lacorre, P. Crystal structure of La$_2$Mo$_2$O$_9$, a new fast oxide−ion conductor. *Chem. Mater.* **2000**, *12*, 2575−2580.

(35) Cortese, A. J.; Abeysinghe, D.; Wilkins, B.; Smith, M. D.; Rassolov, V.; zur Loye, H.-C. Oxygen Anion Solubility as a Factor in Molten Flux Crystal Growth, Synthesis, and Characterization of Four New Reduced Lanthanide Molybdenum Oxides: Ce$_{4.918(3)}$Mo$_3$O$_{16}$, Pr$_{4.880(3)}$Mo$_3$O$_{16}$, Nd$_{4.910(3)}$Mo$_3$O$_{16}$, and Sm$_{4.952(3)}$Mo$_3$O$_{16}$. *Cryst. Growth Des.* **2016**, *16*, 4225−4231.

(36) Jacas Biendicho, J.; Playford, H. Y.; Rahman, S. M. H.; Norberg, S. T.; Eriksson, S. G.; Hull, S. The Fluorite-Like Phase Nd$_5$Mo$_3$O$_{16±δ}$ in the MoO$_3$−Nd$_2$O$_3$ System: Synthesis, Crystal Structure, and Conducting Properties. *Inorg. Chem.* **2018**, *57*, 7025−7035.

(37) Naruke, H.; Yamase, T. Structural investigation of R$_2$Mo$_4$O$_{15}$ (R= La, Nd, Sm), and polymorphs of the R$_2$Mo$_4$O$_{15}$ (R= rare earth) family. *J. Solid State Chem.* **2003**, *173*, 407−417.

(38) Deng, H.; Zhao, Z.; Wang, J.; Hei, Z.; Li, M.; Noh, H. M.; Jeong, J. H.; Yu, R. Photoluminescence properties of a new orange−red emitting Sm^{3+}-doped Y$_2$Mo$_4$O$_{15}$ phosphor. *J. Solid State Chem.* **2015**, *228*, 110−116.

(39) Du, P.; Yu, J. S. Near-Infrared Light-Triggered Visible Upconversion Emissions in Er^{3+}/Yb^{3+}-Codoped Y$_2$Mo$_4$O$_{15}$ Micro-particles for Simultaneous Noncontact Optical Thermometry and Solid-State Lighting. *Ind. Eng. Chem. Res.* **2018**, *57*, 13077−13086.

(40) Naruke, H.; Yamase, T. Crystallization and structural characterization of two europium molybdates, Eu$_4$Mo$_7$O$_{27}$ and Eu$_6$Mo$_{10}$O$_{39}$. *J. Solid State Chem.* **2001**, *161*, 85−92.

(41) Naruke, H.; Yamase, T. Structures of Novel R$_2$Mo$_5$O$_{18}$ and R$_6$Mo$_{12}$O$_{45}$ (R = Eu and Gd) Prepared by Thermal Decomposition of Polyoxomolybdate Precursor [R$_2$(H$_2$O)$_{12}$Mo$_8$O$_{27}$]·nH$_2$O. *Inorg. Chem.* **2002**, *41*, 6514−6520.

(42) Vu, T.; Krichen, F.; Barre, M.; Coste, S.; Jouanneaux, A.; Suard, E.; Fitch, A.; Goutenoire, F. Ab initio structure determination of La$_{34}$Mo$_8$O$_{75}$ using powder X-ray and neutron diffraction data. *Cryst. Growth Des.* **2019**, *19*, 6074−6081.

(43) *Inorganic Crystal Structure Database*, https://icsd.fiz-karlsruhe.de.

(44) Rodríguez-Carvajal, J. Recent Advances in Magnetic Structure Determination by Neutron Powder Diffraction. *Phys. B Condens. Matter* **1993**, *192*, 55−69. The complete program and documentation can be obtained in http://www.ill.eu/sites/fullprof/

(45) Runčevski, T.; Brown, C. M. The Rietveld refinement method: Half of a century anniversary. *Cryst. Growth Des.* **2021**, *21*, 4821−4822.

(46) Le Bail, A. Whole powder pattern decomposition methods and applications: A retrospection. *Powder Diffr.* **2005**, *20*, 316−326.

(47) Thompson, P.; Cox, D. E.; Hastings, J. B. Rietveld Refinement of Debye−Scherrer Synchrotron X-Ray Data from Al$_2$O$_3$. *J. Appl. Crystallogr.* **1987**, *20*, 79−83.

(48) Bandurkin, G. A.; Chudinova, N. N.; Lysanova, G. V.; Krut'ko, V. A.; Komova, M. G.; Balagina, G. M. Nanostructural oxide "memory" of rare earth molybdates. *Russ. J. Inorg. Chem.* **2007**, *52*, 1081−1087.

(49) González-Silgo, C.; Torres, M. E.; Sabalisck, N. P.; Martín-Mateos, I. T.; Zanardi, E.; Mujica, A.; Lahoz, F.; López-Solano, J.; Guzmán-Afonso, C. *Polarons: Recent Progress and Perpectives*; Laref, A., Ed.; Nova Science, 2018; pp 305−363.

(50) Nylund, I.-E.; Tsoutsouva, M.; Grande, T.; Meier, D. Observation of cation-specific critical behavior at the improper ferroelectric phase transition in Gd$_2$(MoO$_4$)$_3$. *Phys. Rev. Mater.* **2022**, *6*, 034402.

(51) Komornicka, D.; Wołcyrz, M.; Pietraszko, A. Polymorphism and polytypism of α-LiNH$_4$SO$_4$ crystals. Monte Carlo modeling based on X-ray diffuse scattering. *Cryst. Growth Des.* **2014**, *14*, 5784−5793.

(52) Sabalisck, N. P.; Guzmán-Afonso, C.; González-Silgo, C.; Torres, M. E.; Pasán, J.; del-Castillo, J.; Ramos-Hernández, L.; Hernández-Suárez, A.; Mestres, L. Structures and thermal stability of the α-LiNH$_4$SO$_4$ polytypes doped with Er^{3+} and Yb^{3+}. *Acta Crystallogr.* **2017**, *73*, 122−133.

(53) Stokes, H. T.; Hatch, D. M. Procedure for obtaining microscopic mechanisms of reconstructive phase transitions in crystalline solids. *Phys. Rev. B: Condens. Matter Mater. Phys.* **2002**, *65*, 144114.

(54) Sabalisck, N.; Gil-de-Cos, G.; González-Silgo, C.; Guzmán-Afonso, C.; Lavín, V.; López-Solano, J.; Martín-Mateos, I. T.; Mestres, L.; Mujica, A.; Santamaría-Pérez, D.; Torres, M. E.; Vendrell, X. Role of Rare Earth Sites and Vacancies in the Anomalous Compression of Modulated Scheelite Tungstates RE$_2$(WO$_4$)$_3$. *Phys. Rev. Mater.* **2021**, *5*, 123601.

(55) Gomez-Villalba, L. S.; López-Arce, P.; Alvarez de Buergo, M.; Fort, R. Atomic defects and their relationship to aragonite−calcite transformation in portlandite nanocrystal carbonation. *Cryst. Growth Des.* **2012**, *12*, 4844−4852.